Published by
NIGERIAN SOCIETY OF PHYSICAL SCIENCES
Available online @ https://journal.nsps.org.ng/index.php/jnsps

J. Nig. Soc. Phys. Sci. 7 (2025) 2936

Journal of the Nigerian Society of Physical Sciences

Hydrodynamic Casson hybrid nanofluid flow across a stretching sheet in the regime of velocity slip and temperature jump, including viscous dissipation, melting, Soret and Dufour effects

B. Laxmi[a], K. Chand[a], P. Thakur[b,*]

[a]*Department of Mathematics & Statistics, Himachal Pradesh University, Summer Hill, Shimla-171005, India*
[b]*Department of Mathematics, ICFAI University, Himachal Pradesh, Solan, India*

Abstract

This work explores the magnetohydrodynamics (MHD) viscous, incompressible, Casson hybrid nanofluid over a stretched sheet which is a well-known non-Newtonian fluid. The analysis incorporates the effects of viscous dissipation, melting, Soret and Dufour effects, within the frameworks of velocity slip and temperature jump boundary conditions. Copper (Cu) and alumina oxide (Al_2O_3) have been employed as nanoparticles, while water (H_2O) has been considered as the base fluid. This mixture is used to increase the fluid's thermal characteristics for better heat transfer efficiency. To simplify the complex governing partial differential equations describing the flow and heat transfer characteristics, similarity transformations were employed, which reduced the system to a set of coupled, ordinary differential equations that are nonlinear. The bvp4c function in MATLAB was used to solve these modified equations numerically. The study looks into the effects of various parameters on flow and heat transfer characteristics, such as the volume fractions of alumina and copper, the Prandtl Number, the Radiation parameter, the Darcy permeability, the Magnetic field parameter, the heat source/sink parameter, melting parameter, the Eckert Number, the Soret number, and the Dufour number. Results indicate that the alumina volume fraction influences the velocity, temperature and concentration profiles. Specifically, the aluminium oxide volume fraction parameter causes increases in profiles of temperature, velocity and concentration. With suction and the Casson parameter, the mass transfer rate increases while the heat transfer rate decreases.

DOI:10.46481/jnsps.2025.2936

Keywords: Magnetohydrodynamics, Viscous dissipation, Casson hybrid nanofluid, Soret and Dufour number, Stretching sheet

Article History :
Received: 16 March 2025
Received in revised form: 09 July 2025
Accepted for publication: 15 July 2025
Available online: 30 July 2025

Communicated by: B. J. Falaye

Nomenclature

u - velocity in the x-direction
v -velocity in the y-direction
u_w - surface velocity
v_w - wall mass transfer velocity
g - acceleration due to gravity
ψ - stream function
L - characteristic length
K_1 - velocity slip factor
K_2 - thermal slip factor
K_3 - concentration slip factor
β - Non-Newtonian Casson parameter
B_0 - constant applied magnetic field
T - fluid temperature
T_w - varying temperature of the surface
T_∞ - free stream temperature

*Corresponding author Tel. No.: +91-857-097-5865.
Email address: pankaj@journal.nsps.org.ng (P. Thakur)

η - dimensionless similarity variable
Me - melting surface parameter
S - suction parameter (also used for wall mass transfer)
f - dimensionless velocity
θ - dimensionless temperature
ϕ - dimensionless concentration
Sc - Schmidt number
R - radiation parameter
Pr - Prandtl number
Ec - Eckert number
C_f - local skin friction coefficient
Nu_x - local Nusselt number
Sh_x - local Sherwood number
Q - heat source/sink parameter
ρ_f - fluid density
k_f - thermal conductivity of fluid
ρ_{hnf} - density of hybrid nanofluid
$(\rho C_p)_f$ - heat capacity of fluid
$(\rho C_p)_{hnf}$ - heat capacity of hybrid nanofluid
μ_f - dynamic viscosity of fluid
μ_{hnf} - dynamic viscosity of hybrid nanofluid
A - dimensionless velocity slip parameter
B - dimensionless thermal slip parameter
C - dimensionless concentration slip parameter
M - dimensionless magnetic field parameter
σ_f - electrical conductivity of fluid
σ_{hnf} - electrical conductivity of hybrid nanofluid
β_f - thermal expansion coefficient of fluid
β_{hnf} - thermal expansion coefficient of hybrid nanofluid
β_{s1} - thermal expansion coefficient of alumina
β_{s2} - thermal expansion coefficient of copper
k_{hnf} - thermal conductivity of hybrid nanofluid
ϕ_{s1} - nanoparticle volume fraction of alumina
ϕ_{s2} - nanoparticle volume fraction of copper
Sr - Soret number
Du - Dufour number
τ - shear stress
D_{hnf} - mass diffusivity of hybrid nanofluid
D_f - mass diffusivity of base fluid.

1. Introduction

Nanofluids are sophisticated fluids that contain finely dispersed micro-sized particles (less than 100 nanometers) in a fluid, like ethylene glycol, water, or oil. These nanoparticles, which are frequently metals or metal oxides, significantly increase the heat transfer capability of the fluids, thereby enhancing heat convection and conduction. The demand for creative heat transfer solutions is rising as a result of recent technological developments. The advantages of nanofluids for engineering and manufacturing applications have been demonstrated by an increase in research on them. Heat transfer capability of the nanoparticles, their concentration ratio and the flow rate are the primary determinants of how well nanofluids transfer heat. The crucial element is the nanoparticles thermal conductivity at constant particle concentrations and flow rates. By combining various materials at the nanoscale to create hybrid nanoparticles, this conductivity can be increased. These composite nanoparticles are used in hybrid nanofluids, which have demonstrated promise but also pose novel difficulties that are currently being investigated by scientists. Casson fluids exhibit shear-thinning behavior and yield stress, making them non-Newtonian fluids whose flow characteristics alter under stress. Casson fluid has numerous real-life applications, particularly in food processing, the cosmetics industry, engineering and manufacturing, oil and gas industry etc. The behaviour of Casson fluids is seen in food products such as chocolate syrup and tomato sauce.

An analytical solution of boundarty layer flow along stretching plate was provided by Crane [1] and Wang [2], they investigated the changes in boundary layer flow over surfaces that deforms linearly. The behavior of transport effects for reactive chemical components on an expanding surface was highlighted by Andersson *et al.* [3]. Choi and Eastman [4] were the first to investigate nanofluids and discovered that hybrid nanofluids improve heat conductivity and transfer rates. Concerns about their development, stability, characterization, and applications require further investigation. In order to understand the behavior of Casson fluids in industrial processes like coating and stretching, one must understand how they flow over a stretching surface. The Casson model, which was first presented by Casson [5], describes these fluids and includes properties like shear resistance at elevated rates, yield stress, and shear thinning. Using the Casson and Carreau-Yasuda models, Boyd *et al.* [6] investigated Newtonian and non-Newtonian oscillatory fluid flows in steady and curved pipes by using the Lattice-Boltzmann method.

Mukhopadhyay *et al.* [7] analysed the 2-D Casson fluid moving across moving across an unsteady stretching sheet. Pramanik [8] conducted a study on the boundary layer flow of a Casson fluid that includes the impact of heat radiation over an exponential expanded surface. Devi and Devi [9] examined the flow of hybrid nanofluids with $Cu - Al_2O_3$/water using computational methods. They discovered that in order to increase heat transfer efficiency, oxide nanoparticles which have a lower heat conductivity than metallic ones must be used in larger volumes. Hayat *et al.* [10] evaluate the characteristics of CuO/H_2O and $Ag - CuO/H_2O$ nanofluids' heat transfer characteristics on a stretched boundary while taking reactive flow and radiant heat into account. Using the impacts of Soret and Dufour phenomena, Reddy and Krishna [11] investigated the flow behavior of a magnetohydrodynamic (MHD) micropolar fluid across a stretched sheet through a non-Darcy porous material. Shojaei *et al.* [12] have investigated the flow characteristics of a second-order fluid over a radiatively expanding cylinder, taking into consideration cross-diffusion and both the effects of Soret and Dufour. Reddy *et al.* [13] have investigated how MHD flows of a Casson fluid across an angled porous expanding surface.

Understanding how the thermodynamic melting process works in fluid flow is crucial for many real-world applications. This knowledge is important in various fields, including the melting of permafrost, the solidification of magma, metal purification, semiconductor manufacturing, and welding. For instance, in designing and optimizing heat exchangers, where a solid melts due to heat exchange in flowing fluid effectively.

Nandeppanavar [14] used a moving plate to study the behavior of melting heat exchange in Casson fluid. In a study on MHD boundary layer flow, Jawad *et al.* [15] took into account a Darcy-Forchheimer radiative nanofluid that combined the consequences of Soret and Dufour. Malik *et al.* [16] have investigated the effects of heat diffusion during melting through Sisko fluid forced convection. Furthermore, research has demonstrated the melting transfer of heat for a variety of fluids and geometries. A thorough investigation of the melting behavior of heat transmission in Casson fluid flow across a stretching sheet was carried out by Sharma *et al.* [17]. Their analysis took into account the joint effect of Dufour and Soret as well as the impact of velocity and the circumstances of thermal slippage. Ali *et al.* [18] studied theoretically the MHD Casson composite nanofluid in a porous medium, which is assumed to be unstable.

Motivated by earlier studies, the current work investigates the magnetohydrodynamic (MHD) flow of a viscous, incompressible Casson composite nanofluid on a sheet that is stretching. The study considers the effects of melting, viscous dissipation, Soret and Dufour phenomena, as well as velocity and temperature jump circumstances, to provide a comprehensive analysis of heat and mass transfer characteristics under complicated physical conditions. Here water (H_2O) is utilized as the base fluid, while Alumina (Al_2O_3) and copper (Cu) are chosen as hybrid nanoparticles. The ruling partial differential equations are reduced to ordinary differential equations by using a similarity transformation approach. The MATLAB bvp4c solver, which is a potent tool for resolving boundary value issues, was used to solve the ensuing governing ODEs and in numerical evaluations. Some important parameters occurring in the governing equations are investigated to ascertain their impacts on concentration, velocity and temperature profiles, including the Prandtl number, radiation, Darcy permeability, heat source/sink, melting, magnetic field parameter, Eckert, Dufour and Soret numbers and the volume fractions of alumina and copper. To enable a thorough examination of the flow properties and thermal behavior under various circumstances, those impacts are visually depicted.

2. Mathematical formulation

The linear convective transport of mass and heat in a Casson hybrid nanofluid flowing over a linearly stretched surface is investigated in a steady, two-dimensional study. The y-axis is perpendicular to the x-axis, which indicates the stretching direction. The wall velocity can be expressed as, $u_w(x) = bx$, where $b > 0$ is the stretching rate constant and u_w is the wall velocity. $B(x) = B_0 x$ is the magnetic field's vertical intensity, where B_0 is the applied magnetic induction. As illustrated in Figure 1, we took into consideration the velocity components u and v, which represent the flow directions along the x and y axes, respectively. The temperature, concentration, and fluid velocity of the nanoparticle near the surface are assumed to be U_w, T_w, and C_w, respectively. The stress tensor (τ) of the Casson fluid is defined as follows:

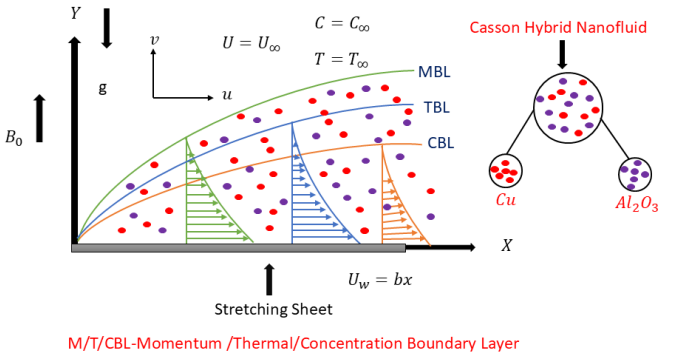

Figure 1: Geometrical configuration of the physical model for stretching surface.

$$\tau_{ij} = \begin{cases} 2\left(\mu + \dfrac{p_y}{\sqrt{2\pi}}\right)e_{ij}, & \pi > \pi_c \\ 2\left(\mu + \dfrac{p_y}{\sqrt{2\pi_c}}\right)e_{ij}, & \pi < \pi_c, \end{cases} \tag{1}$$

where

$$e_{ij} = \frac{1}{2}\left(\frac{\partial u_i}{\partial x_j} + \frac{\partial u_j}{\partial x_i}\right),$$

where μ denotes the fluid's viscosity in the context of Casson fluid dynamics, $p_y\left(= \dfrac{\mu\sqrt{2\pi_c}}{\beta}\right)$ yields the yield stress, where β is the Casson fluid parameter, e_{ij} describes the strain rate factors, π_c indicates the critical value in the non-Newtonian model, and $\pi(e_{ij}e_{ij})$ is the multiplication of strain rate components by themselves. Simplifying the equation (1) by using the value of p_y for a Casson fluid, the main rheological (flow-related) equations transform to the following form if $\pi < \pi_c$:

$$\tau_{ij} = 2\mu\left(1 + \frac{1}{\beta}\right)e_{ij}, \text{where} \quad \beta = \frac{\mu\sqrt{2\pi_c}}{p_y}. \tag{2}$$

When β becomes very large ($\beta \to \infty$) the non-Newtonian characteristics of the fluid are suppressed, and it begins to exhibit the behavior of a Newtonian fluid, which means it flows in a more typical and predictable manner. Using the above assumptions, along with the Boussinesq approximation (which simplifies the treatment of buoyancy forces),and applying equation (2) the momentum equations regulating the steady flow of Casson nanofluids, along with the related boundary conditions as provided by Patil *et al.* [19] and Olkha and Dadheech [20] are as follows:

$$\frac{\partial u}{\partial x} + \frac{\partial v}{\partial y} = 0, \tag{3}$$

$$u\frac{\partial u}{\partial x} + v\frac{\partial u}{\partial y} = \left(1 + \frac{1}{\beta}\right)\frac{\mu_{hnf}}{\rho_{hnf}}\frac{\partial^2 u}{\partial y^2} - \left(1 + \frac{1}{\beta}\right)\frac{\mu_{hnf}}{\rho_{hnf}k^*}u - \frac{\sigma_{hnf}}{\rho_{hnf}}B_0^2 u, \tag{4}$$

$$u\frac{\partial T}{\partial x}+v\frac{\partial T}{\partial y}=\frac{k_{hnf}}{(\rho c_p)_{hnf}}\frac{\partial^2 T}{\partial y^2}-\frac{1}{(\rho c_p)_{hnf}}\frac{\partial q_r}{\partial y}+\frac{D_m K_T \rho_{hnf}}{C_s(\rho c_p)_{hnf}}\frac{\partial^2 C}{\partial y^2}+\left(1+\frac{1}{\beta}\right)\frac{\mu_{hnf}}{(\rho c_p)_{hnf}}\left(\frac{\partial u}{\partial y}\right)^2+\frac{Q_0}{(\rho c_p)_{hnf}}(T-T_\infty)+\frac{\sigma_{hnf}}{(\rho c_p)_{hnf}}B_0^2u^2, \tag{5}$$

$$u\frac{\partial C}{\partial x}+v\frac{\partial C}{\partial y}=D_{hnf}\frac{\partial^2 C}{\partial y^2}+\frac{D_m K_T}{T_m}\frac{\partial^2 T}{\partial y^2}. \tag{6}$$

The relevant boundary conditions are as follows:

$$\left.\begin{aligned} u &= u_w(x)+K_1\left(1+\frac{1}{\beta}\right)\frac{\partial u}{\partial y},\\ v &= \frac{k}{\rho\left(\beta_m+C_s(T_m-T_0)\right)}\frac{\partial T}{\partial x}-v_m,\\ C &= C_w+K_3\frac{\partial C}{\partial y}, T=T_m+K_2\frac{\partial T}{\partial y}, \quad \text{at } y=0,\\ u &\to 0, \quad T\to T_\infty, \quad C\to C_\infty, \text{as } y\to\infty \end{aligned}\right\}, \tag{7}$$

where C_s the concentration susceptibility, D_m represents the mass diffusion ratio, K_T the thermal diffusion ratio, T_m the melting temperature and K_1, K_2, and K_3 are the velocity, thermal and concentration slip coefficients, respectively. Thermal radiation q_r is modeled by using the Rosseland approximation, which is expressed as follows:

$$q_r=-\frac{4\sigma^*}{3k^*}\frac{\partial T^4}{\partial y}, \tag{8}$$

where σ^* representing the Stefan-Boltzmann constant and k^* representing the Rosseland mean absorption coefficient. Assuming that temperature changes within the fluid flow are negligible and that T^4 can be approximately represented as a linear function of temperature $T^4=4T_\infty^3T-3T_\infty^4$, so that equation (8) can be recast as follows:

$$\frac{\partial q_r}{\partial y}=-\frac{16\sigma^*T_\infty^3}{3k^*}\frac{\partial^2 T}{\partial y^2}. \tag{9}$$

The transformed energy equation is obtained by substituting equation (9) into equation (5):

$$u\frac{\partial T}{\partial x}+v\frac{\partial T}{\partial y}=\frac{k_{hnf}}{(\rho c_p)_{hnf}}\frac{\partial^2 T}{\partial y^2}+\frac{16\sigma^*T_\infty^3}{3k^*(\rho c_p)_{hnf}}\frac{\partial^2 T}{\partial y^2}+\frac{D_m K_T\rho_{hnf}}{C_s(\rho c_p)_{hnf}}\frac{\partial^2 C}{\partial y^2}+\left(1+\frac{1}{\beta}\right)\frac{\mu_{hnf}}{(\rho c_p)_{hnf}}\left(\frac{\partial u}{\partial y}\right)^2+\frac{Q_0}{(\rho c_p)_{hnf}}(T-T_\infty)+\frac{\sigma_{hnf}B_0^2u^2}{(\rho c_p)_{hnf}}. \tag{10}$$

The following transformations of similarity are employed to non-dimensionalize the above set of PDEs and transform them into ODEs:

$$\left.\begin{aligned} u &= bxf'(\eta),\\ v &= -\sqrt{b\nu_f}f(\eta),\\ \phi &= \frac{C-C_\infty}{C_w-C_\infty}, \theta=\frac{T-T_\infty}{T_m-T_\infty},\\ \eta &= y\sqrt{\frac{b}{\nu_f}}, \end{aligned}\right\}. \tag{11}$$

It is now observed that the continuity equation (3) is satisfied identically by using equation (11). The remaining dimensional equations (4), (6) and (10) along with the boundary condtions equation (7) by applying equation (11) transform to the following nondimensional equations:

$$\left(1+\frac{1}{\beta}\right)\left(\frac{\mu_{hnf}\rho_f}{\mu_f\rho_{hnf}}\right)f'''+ff''-K\left(1+\frac{1}{\beta}\right)\left(\frac{\mu_{hnf}\rho_f}{\mu_f\rho_{hnf}}\right)f'-f'^2-M\left(\frac{\sigma_{hnf}\rho_f}{\sigma_f\rho_{hnf}}\right)f'=0, \tag{12}$$

$$\frac{1}{Pr}\frac{(\rho C_p)_f}{(\rho C_p)_{hnf}}\left(\frac{k_{hnf}}{k_f}+\frac{4}{3}R\right)\theta''+f\theta'+\frac{(C_p)_f\rho_{hnf}}{(\rho C_p)_{hnf}}Du\,\phi''+\left(1+\frac{1}{\beta}\right)\frac{\mu_{hnf}}{\mu_f}\frac{(\rho C_p)_f}{(\rho C_p)_{hnf}}Ec\,(f'')^2+Q\theta+\frac{\sigma_{hnf}}{\sigma_f}\frac{(\rho C_p)_f}{(\rho C_p)_{hnf}}MEc\,(f')^2=0, \tag{13}$$

$$\phi''+\frac{D_f}{D_{hnf}}Sc\,f\phi'+\frac{D_f}{D_{hnf}}Sc\,Sr\,\theta''=0. \tag{14}$$

The modified boundary conditions becomes:

$$\left.\begin{aligned} &f'(0)=1+A\left(1+\frac{1}{\beta}\right)f''(0), \phi(0)=1+C\phi'(0),\\ &f(0)=S-\frac{Me}{Pr}\theta'(0), \theta(0)=1+B\theta'(0), \quad \text{at} \quad \eta=0\\ &f'(\eta)\to 0, \quad \theta(\eta)\to 0, \quad \phi(\eta)\to 0 \quad \text{as} \quad \eta\to\infty \end{aligned}\right\}, \tag{15}$$

where $\beta=\frac{\mu\sqrt{2\pi}}{p_y}$ is the Casson parameter that is not Newtonian, $S=\frac{v_0}{\sqrt{b\nu_f}}$ represents the mass transfer parameter, the Prandtl number is $Pr=\frac{(\mu C_p)_f}{k_f}$, $M=\frac{\sigma_f B_0^2}{\rho b}$ is the parameter for the magnetic field, $K=\frac{\mu_f}{\rho_f bk^*}$ is the permeability parameter, $R=\frac{4\sigma^*T_\infty^3}{kk^*}$ is the radiation parameter, $Du=\frac{D_mK_T(C_w-C_\infty)}{C_s(\rho C_p)_f\nu_f(T_w-T_\infty)}$ is the Dufour number, the Eckert number is $Ec=\frac{u_w^2}{(T_w-T_\infty)(C_p)_f}$, $Q=\frac{Q_0}{(\rho C_p)_{\text{hnf}}}$ is the parameter for the heat source/sink. $Sc=\frac{\nu_f}{D_f}$ is the Schmidt number, $Sr=\frac{D_mK_T(T_w-T_\infty)}{T_m\nu_f(C_w-C_\infty)}$ is the Soret number, $Me=\frac{(T_m-T_\infty)C_p}{\beta_m+C_s(T_m-T_0)}$ represents the melting surface parameter $A=K_1\sqrt{\frac{b}{\nu_f}}$ is the velocity slip parameter, $B=K_2\sqrt{\frac{b}{\nu_f}}$ is the parameter for thermal slip and $C=K_3\sqrt{\frac{b}{\nu_f}}$ is the mass slip parameter.

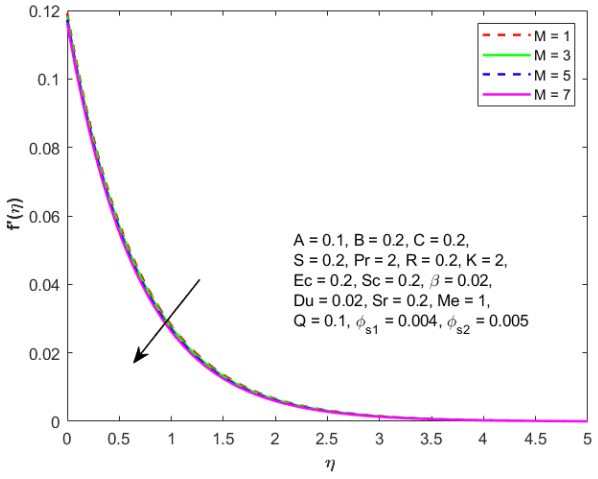

Figure 2: Impact of magnetic field parameter M on $f'(\eta)$.

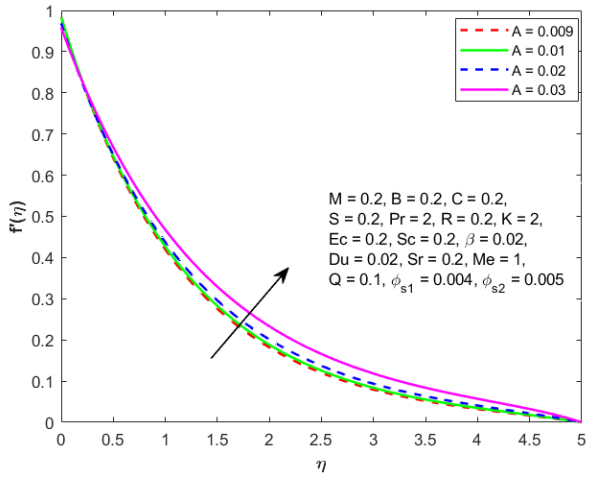

Figure 4: Impact of slip parameter A on $f'(\eta)$.

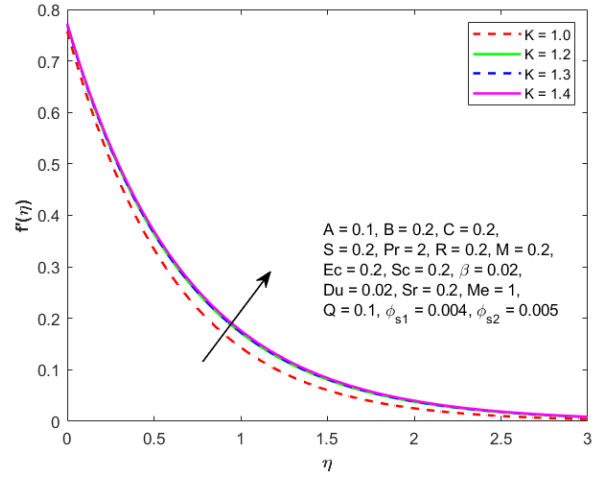

Figure 3: Impact of permeability parameter K on $f'(\eta)$.

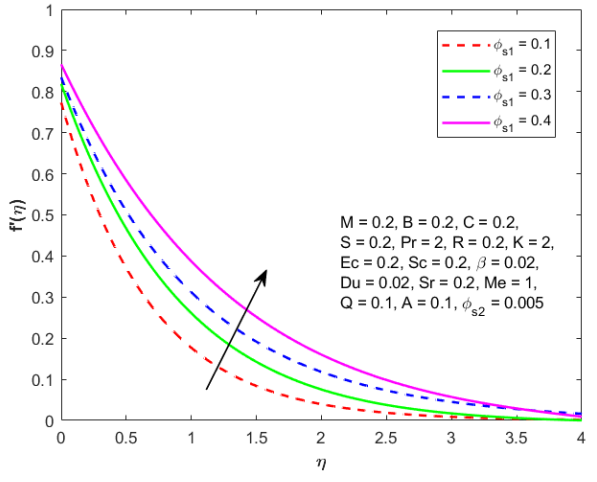

Figure 5: Impact of volume fraction parameter ϕ_{s1} on $f'(\eta)$.

3. Some important physical quantities of the flow field

3.1. Local skin friction coefficient

$$C_f = \frac{\tau_w}{\rho U_w^2}, \text{where} \quad \tau_w = \mu_{hnf}\left(1+\frac{1}{\beta}\right)\left.\frac{\partial u}{\partial y}\right|_{y=0}. \tag{16}$$

By applying equation (11) to equation (16), the local skin friction coefficient in terms of transformed variables can be written as follows:

$$(Re_x)^{1/2} C_f = \frac{\mu_{hnf}}{\mu_f}\left(1+\frac{1}{\beta}\right) f''(0). \tag{17}$$

3.2. The dimensionless coefficient of heat transfer (Nusselt number)

The local Nusselt number's dimensionless representation is provided by:

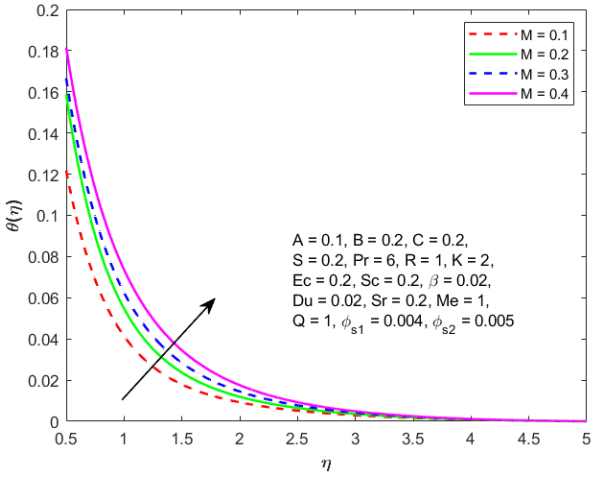

Figure 6: Impact of magnetic field parameter M on $\theta(\eta)$.

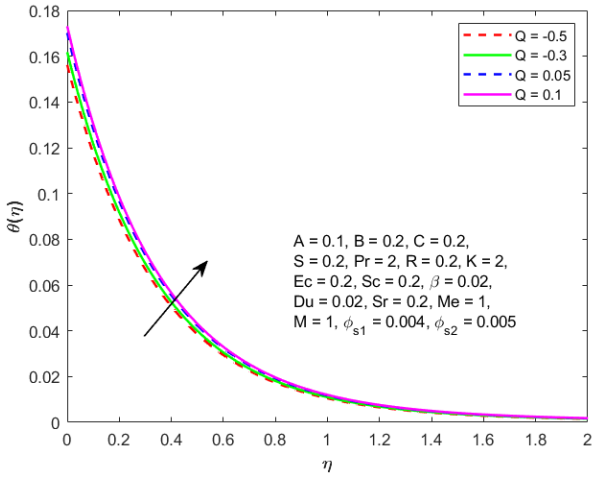

Figure 7: Impact of heat source/sink parameter Q on $\theta(\eta)$.

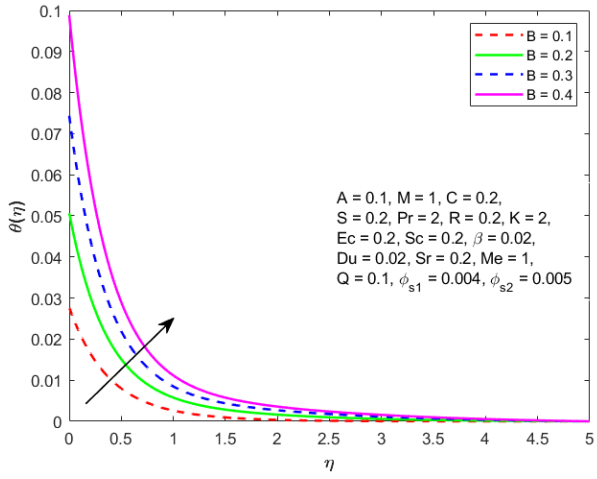

Figure 10: Impact of thermal slip parameter B on $\theta(\eta)$.

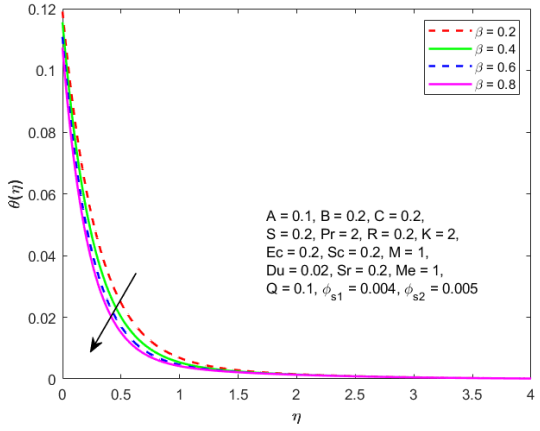

Figure 8: Impact of Casson parameter β on $\theta(\eta)$

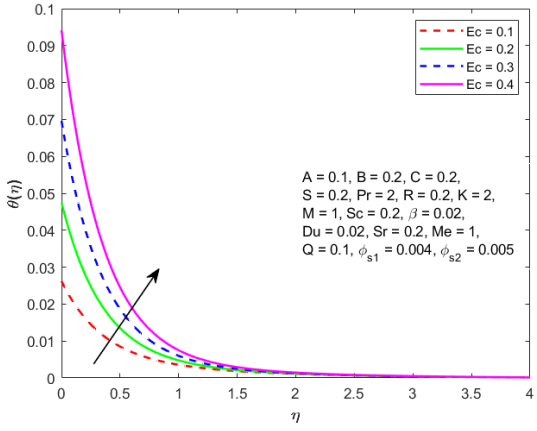

Figure 11: Impact of Eckert number Ec on $\theta(\eta)$

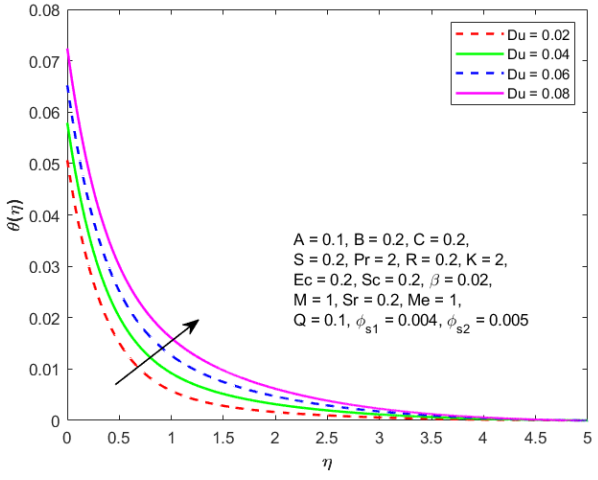

Figure 9: Impact of Dufour number Du on $\theta(\eta)$.

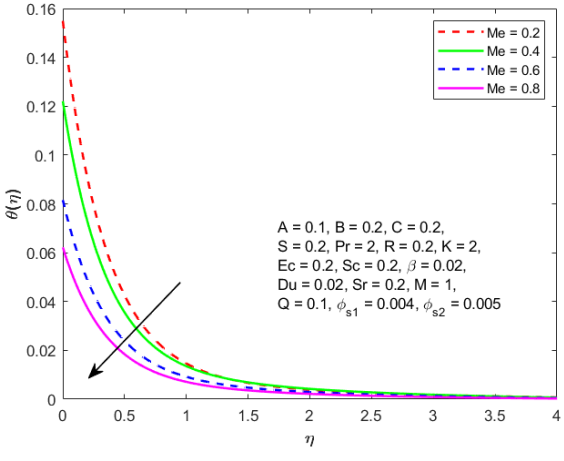

Figure 12: Impact of melting heat transfer parameter Me on $\theta(\eta)$.

$$Nu_x = \frac{xq_w}{k_f(T_w - T_\infty)}, \text{where } q_w = -k_{hnf}\left.\frac{\partial T}{\partial y}\right|_{y=0}. \quad (18)$$

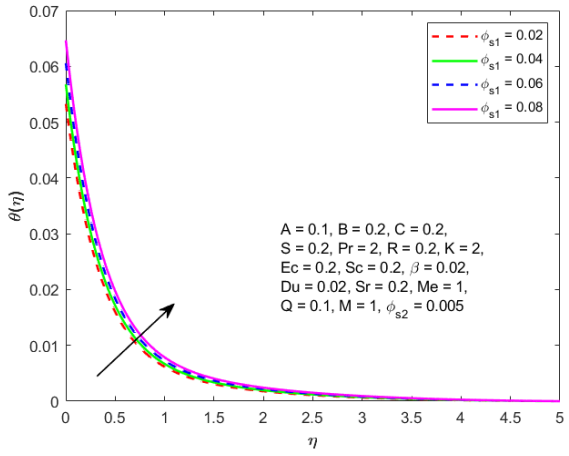

Figure 13: Impact of volume fraction parameter ϕ_{s1} on $\theta(\eta)$.

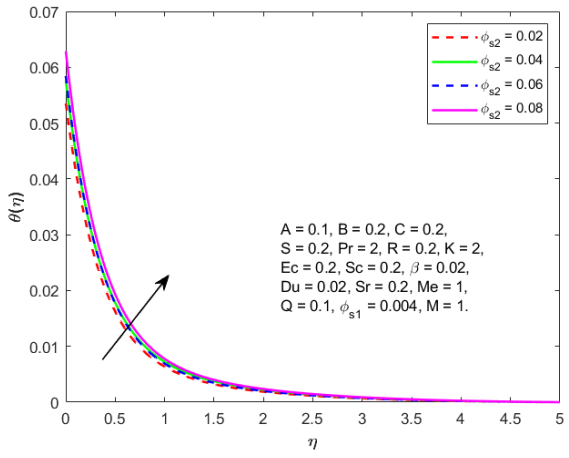

Figure 14: Impact of volume fraction parameter ϕ_{s2} on $\theta(\eta)$,

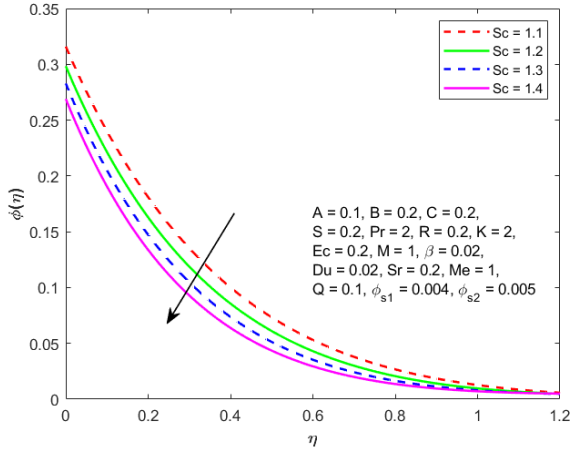

Figure 15: Impact of Schmidt number Sc on $\phi(\eta)$.

From equation (11), the dimensionless expression for the local Nusselt number in terms of transformed variables, and

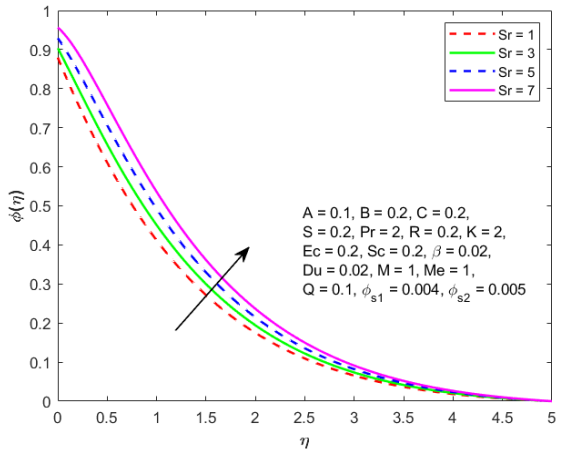

Figure 16: Impact of Soret number Sr on $\phi(\eta)$.

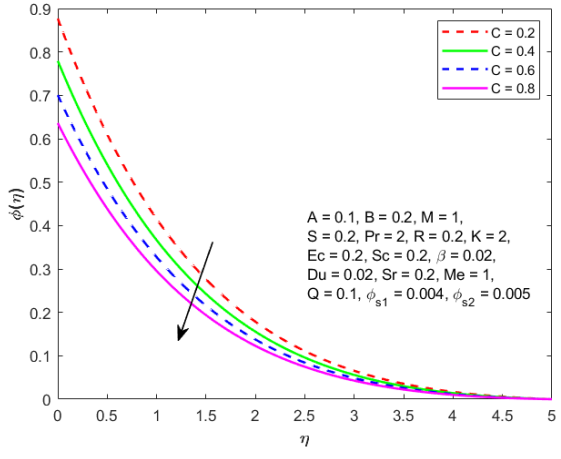

Figure 17: Impact of concentration slip parameter C on $\phi(\eta)$.

equation (18) proved to be:

$$(Re_x)^{-1/2}\, Nu_x = -\frac{k_{hnf}}{k_f}\theta'(0). \tag{19}$$

3.3. *The dimensionless coefficient of mass transfer (Sherwood number)*

The dimensionless expression for the local Sherwood number is given by:

$$Sh_x = \frac{xq_m}{D_f(C_w - C_\infty)}, \text{where } q_m = -D_{hnf}\left.\frac{\partial C}{\partial y}\right|_{y=0}. \tag{20}$$

Substituting equation (11) in equation (20) the dimensionless expression for local Sherwood number in terms of transformed variables turned out to be

$$(Re_x)^{-1/2}\, Sh_x = -\frac{D_{hnf}}{D_f}\phi'(0), \tag{21}$$

where $Re_x = \frac{bx^2}{\nu_f}$ is the local Reynolds number, in this instance, $f''(0), \theta'(0)$, and $\phi'(0)$ can be obtained using equations (12)-(14).

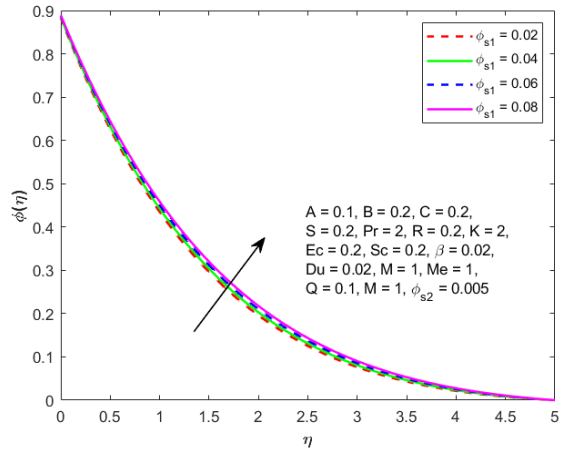

Figure 18: Impact of volume fraction parameter ϕ_{s1} on $\phi(\eta)$.

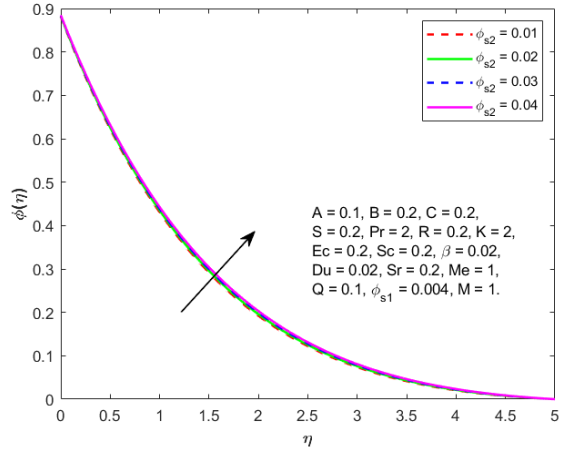

Figure 19: Impact of volume fraction parameter ϕ_{s2} on $\phi(\eta)$.

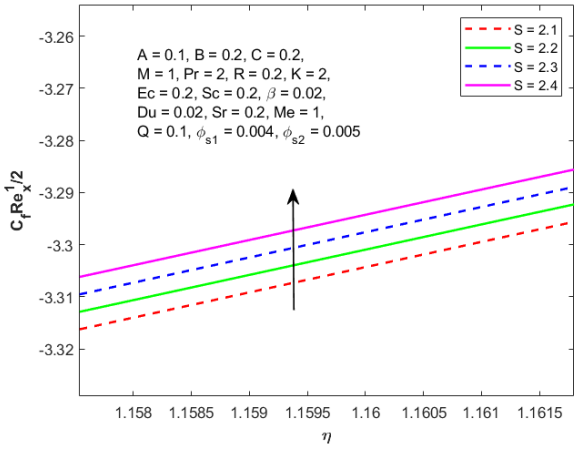

Figure 20: Effect of velocity suction parameter S on skin friction coefficient.

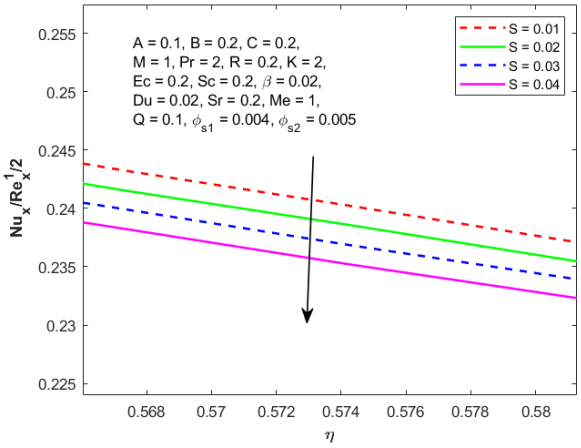

Figure 21: Effect of velocity suction parameter S on Nusselt number.

4. Results and discussion

This study examines how the flow of a Casson hybrid nanofluid is affected by viscous deformation, melting, Soret, and Dufour phenomena, as well as temperature jump, velocity and concentration slip boundary conditions. To make the hybrid nanofluid, also called $Cu - Al_2O_3$/water nanofluid, alumina $Al_2O_3(\phi_{s1})$ and copper $Cu(\phi_{s2})$ nanoparticles are dispersed in water at varying solid volume fractions. Equations (12)-(14) by using the boundary conditions given by equation (15) are solved by using MATLAB's bvp4c solver. The graphs are also utilized to illustrate the impact of pertinent parameters on fluid profiles for momentum $f'(\eta)$, energy $\theta(\eta)$ and mass diffussion $\phi(\eta)$. Numerous physical parameters, such as the Casson fluid β, permeability K, magnetic field M, Dufour Du, Soret Sr and Prandtl number Pr, radiation parameter R, Eckert number Ec and Schmidt number Sc, heat source/sink Q, melting Me, velocity slip A, thermal slip B, and mass slip C, as well as the nanoparticle volume fractions ϕ_{s1} and ϕ_{s2} have been numerically evaluated and further applied to evaluate the various important characteristics of the flow field. The equation (17), equation (19) and equation (21) are used to get the local skin friction coefficient (C_f), mass transfer rate and heat exchange rate, respectively.

4.1. Impact on velocity profile $f'(\eta)$

An increase in the magnetic field parameter (M) has a considerable effect on fluid flow, as seen in Figure 2. An opposing force known as the Lorentz force is created when the fluid's electrical impulses interact with the magnetic field. The fluid's velocity continues to decline when this force intersects the flow. Increasing the porosity parameter (K) also affects the fluid's velocity, as seen in Figure 3. The graphic makes it clear that velocity rises with the permeability parameter. Because of the increased permeability, the fluid encounters less drag force. As a result, the fluid can move more freely, leading to higher velocities. The investigation of the impact of the velocity slip

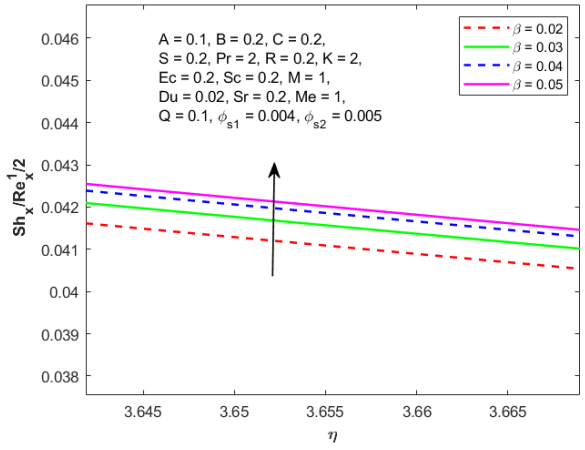

Figure 22: Effect of Casson parameter β on Sherwood number.

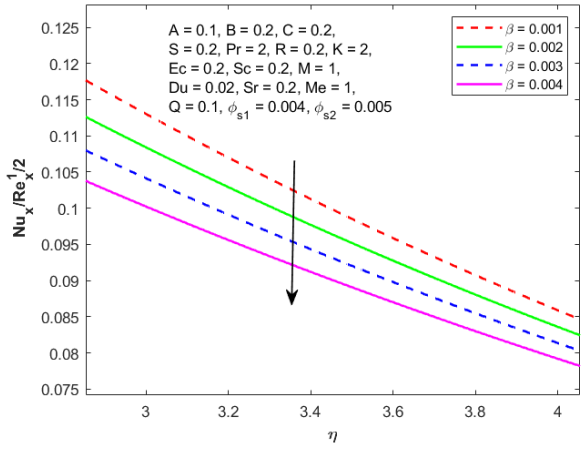

Figure 23: Effect of Casson parameter β on Nusselt number.

parameter (A) on the velocity profile $f'(\eta)$ is shown in Figure 4. The figure makes it evident that as the velocity slip parameter increases, so does the velocity profile. This is explained by the fact that velocity slip at the shrinking surface boundaries lowers flow resistance and consequently increases the flow velocity by letting more flow through the surface. Figure 5 illustrates that how increasing aluminum oxide volume fraction parameter (ϕ_{s1}) raises the velocity profile $f'(\eta)$. This occurs because the addition of a hybrid nanofluid, such as aluminum oxide, to water enhances the fluid's thermal characteristics, including its heat transfer coefficient, thermal diffusivity, and thermal conductivity, all of which raise the velocity profile.

4.2. *Impact on temperature profile $\theta(\eta)$*

A change in the magnetic field (M) affects the temperature in a convection system, as shown in Figure 6. As the magnetic field gets stronger, the fluid's temperature rises because the magnetic damping transforms the fluid's kinetic energy into heat. Figure 7 illustrates how increasing the number of heat source/sink parameters (Q) affects heat transfer. The temperature rises as Q rises because more heat generation results in a wider temperature spread. Figure 8, illustrates how the Casson parameter (β) affects the temperature profile which demonstrates that a rise in β lowers the temperature. The temperature drops as β rises because of the slower heat transfer caused by the increased viscosity. Figure 9 illustrates how temperature changes as the Dufour number (Du) increases. Higher heat transfer rates result from Du increasing viscosity and decreasing fluid resistance. The effect of the thermal slip parameter B on the temperature $\theta(\eta)$ is depicted in Figure 10. It is discovered that the temperature field rises in tandem with the slip parameter. Figure 11 shows how the Eckert number (Ec) affects the temperature profile $\theta(\eta)$. It is clear that as the Eckert number rises, the temperature profile along the stretching sheet climbs as well. The behavior of temperature distributions at higher values of the melting heat Me transfer is seen in Figure 12. It has been found that when the melting heat transfer is increased, the fluid flows more quickly, lowering the temperature profile. $\theta(\eta)$ increases when the aluminum oxide volume fraction ϕ_{s1} and copper volume fraction ϕ_{s2} are raised, as seen in Figure 13 and Figure 14.

4.3. *Impact on concentration profile $\phi(\eta)$*

The impact of the Schmidt number Sc on mass dissipation is depicted in Figure 15, due to the border layer of concentration becoming narrower as a result of the commensurate drop in mass diffusivity. Figure 16 depicts how the concentration profile is affected by the Soret number Sr. The Soret number relates the temperature difference to the concentration difference. As Sr increases, the temperature gradient becomes steeper, which likely speeds up molecular diffusion. Consequently, with higher Soret numbers mass transfer rates increase and $\phi(\eta)$ improves. Figure 17 illustrates the impact of the concentration slip parameter C. This shows that the slip slows down fluid movement, which reduces molecular movement. As a result, both temperature and mass fraction decrease. Figures make this clear that the $\phi(\eta)$ improves when the copper volume fraction parameter ϕ_{s2} and the aluminum oxide volume fraction parameter ϕ_{s1} rise, according to Figure 19 and Figure 18.

4.4. *Impact on skin friction (C_f), local Nusselt number (Nu_x) and local Sherwood number (Sh_x)*

Figure 20 shows that the skin friction coefficient $\sqrt{\mathrm{Re}_x}\,C_f$ improves with increased suction (S) as the velocity profile improves as the suction increases and the momentum boundary layer thins. $\frac{\mathrm{Nu}_x}{\sqrt{\mathrm{Re}_x}}$, which represents the surface heat transfer rate, falls as the suction parameter increases it is expressed in Figure 21. For a variety of Casson fluid parameter (β) values, the mass transfer rate $\frac{\mathrm{Sh}_x}{\sqrt{\mathrm{Re}_x}}$ is displayed in Figure 22. The fluid gets viscous and the Sherwood number decreases as the Casson fluid parameter increases. In Figure 23, the heat transfer rate $\frac{\mathrm{Nu}_x}{\sqrt{\mathrm{Re}_x}}$ is shown against the Casson parameter. The graphic clearly shows that a higher heat transfer rate is the result of an increase in β.

5. Conclusion

The viscous, incompressible Casson hybrid nanofluid's magnetohydrodynamic (MHD) flow across a stretching sheet is explored in this study. In addition to velocity and concentration slip along with temperature jump circumstances, the research considers the impacts of melting, viscous dissipation, Soret, and Dufour phenomena. The bvp4c solver was used to solve the PDEs after they were converted into ODEs via similarity transformations. The results obtained are numerically evaluated and expressed with the help of graphs. The primary conclusions of the study can be listed below:

- The analysis shows that the magnetic field (M) has a direct effect on the temperature profile and an inverse effect on the velocity profile. Additionally, increasing the Darcy permeability (K) improves the velocity profile.
- As the Dufour number (Du) grows, the temperature profile $\theta(\eta)$ rises as well, illustrating the role of thermal diffusion in heat transport, whereas the temperature profile $\theta(\eta)$ falls with the Casson fluid parameter (β).
- The heat source/sink (Q), Eckert number (Ec) and thermal slip parameter (B) raise the temperature profile $\theta(\eta)$ along the stretched sheet, while the heat melting parameter (Me) has the opposite effect.
- The copper and aluminum oxide volume fraction parameters ϕ_{s2} and ϕ_{s1} of the hybrid nanofluid increases the velocity, temperature and concentration profiles.
- Higher Soret numbers (Sr) encourage concentration $\phi(\eta)$ fields, whereas increasing Schmidt numbers (Sc) results in a decrease in $\phi(\eta)$.
- The suction (S) increases the skin friction coefficient while decreasing the rate of heat transfer. The Casson fluid parameter (β) raises the skin friction coefficient and the rate of mass transfer while decreasing the rate of heat transfer.

Data availability

The data will be available on request from the corresponding author.

References

[1] L. J. Crane, "Flow past a stretching plate", Zeitschrift für Angewandte Mathematik und Physik **21** (1970) 645. https://doi.org/10.1007/BF01587695.

[2] C. Y. Wang, "Free convection on a vertical stretching surface", Journal of Applied Mathematics and Mechanics **69** (1989) 418. https://doi.org/10.1002/zamm.19890691115.

[3] H. I. Andersson, O. R. Hansen & B. Holmedal, "Diffusion of a chemically reactive species from a stretching sheet", International Journal of Heat Mass Transfer **37** (1994) 659. https://doi.org/10.1016/0017-9310(94)90137-6.

[4] S. U. S. Choi & J. A. Eastman, "Enhancing thermal conductivity of fluids with nanoparticles", Argonne National Lab.(ANL) (1995).

[5] N. Casson, "Flow equation for pigment-oil suspensions of the printing ink-type", in *Rheology of disperse system*, Pergamon Press, New York, USA, 1959, pp. 84.

[6] J. Boyd, J. M. Buick & S. Green, "Analysis of the Casson and Carreau-Yasuda non-Newtonian blood models in steady and oscillatory flows using the lattice Boltzmann method", Physics of Fluids **19** (2007) 093103. https://doi.org/10.1063/1.2772250.

[7] S. Mukhopadhyay, P. R. De, K. Bhattacharyya & G. C. Layek, "Casson fluid flow over an unsteady stretching surface", Ain Shams Engineering Journal **4** (2013) 933. https://doi.org/10.1016/j.asej.2013.04.004.

[8] S. Pramanik, "Casson fluid flow and heat transfer past an exponentially porous stretching surface in presence of thermal radiation", Ain Shams Engineering Journal **5** (2014) 205. https://doi.org/10.1016/j.asej.2013.05.003.

[9] S. P. A. Devi & S. S. U. Devi, "Numerical investigation of hydromagnetic hybrid Cu-Al_2O_3/water nanofluid flow over a permeable stretching sheet with suction", International Journal of Nonlinear Sciences and Numerical Simulation **17** (2016) 249. http://dx.doi.org/10.1515/ijnsns-2016-0037.

[10] T. Hayat & S. Nadeem, "Heat transfer enhancement with Ag-CuO/water hybrid nanofluid", Results in Physics **7** (2017) 2317. https://doi.org/10.1016/j.rinp.2017.06.034.

[11] G. V. R. Reddy & Y. H. Krishna, "Soret and Dufour effects on MHD micropolar fluid flow over a linearly stretching sheet, through a non-darcy porous medium", International Journal of Applied Mechanics and Engineering **23** (2018) 485. http://dx.doi.org/10.2478/ijame-2018-0028.

[12] A. Shojaei, A. J. Amiri, S. S. Ardahaie, K. Hosseinzadeh & D. D. Ganji, "Hydrothermal analysis of non-Newtonian second grade fluid flow on radiative stretching cylinder with Soret and Dufour effects", Case Studies in Thermal Engineering **13** (2019) 100384. https://doi.org/10.1016/j.csite.2018.100384.

[13] K. V. Reddy, G. V. R. Reddy, A. Akgül, R. Jarrar, H. Shanak & J. Asad, "Numerical solution of MHD Casson fluid flow with variable properties across an inclined porous stretching sheet", AIMS Mathematics **12** (2022) 20524. https://doi.org/10.3934/math.20221124.

[14] M. M. Nandeppanavar, "Melting heat transfer analysis of non-Newtonian Casson fluid due to moving plate", Engineering Computations **35** (2018) 1301. https://doi.org/10.1108/EC-04-2017-0148.

[15] M. Jawad, A. Saeed, P. Kumam, Z. Shah & A. Khan, "Analysis of boundary layer MHD Darcy-Forchheimer radiative nanofluid flow with Soret and Dufour effects by means of Marangoni convection", Case Studies in Thermal Engineering **23** (2021) 100792. https://doi.org/10.1016/j.csite.2020.100792.

[16] R. Malik, A. Munir, H. Sadaf & M. Khan, "Melting heat transfer by forced convection of Sisko fluid", Waves in Random and Complex Media **35** (2022) 4761. https://doi.org/10.1080/17455030.2022.2064560.

[17] S. Sharma, M. Goyal & A. Dadheech, "Melting, Soret and Dufour effect on MHD Casson fluid flow over a stretching sheet with slip conditions", Journal of Engineering Mathematics **146** (2024). https://doi.org/10.1007/s10665-024-10364-0.

[18] A. Ali, Rabia, S. Hussain & M. Asharf, "Theoretical investigation of unsteady MHD Casson hybrid nanofluid in porous medium: Application of thermal radiations and nanoparticle", Journal of Radiation Research and Applied Sciences **17** (2024) 101029. https://doi.org/10.1016/j.jrras.2024.101029.

[19] M. B. Patil, K. C. Shobha, S. Bhattacharyya & Z. Said, "Soret and Dufour effects in the flow of Casson nanofluid in a vertical channel with thermal radiation: entropy analysis", Journal of Thermal Analysis and Calorimetry **148** (2023) 2857. https://doi.org/10.1007/s10973-023-11962-3.

[20] A. Olkha & A. Dadheech, "Second law analysis for radiative magnetohydrodynamics slip flow for two different non-Newtonian fluid with heat source", Journal of Nanofluids **10** (2021) 447. http://dx.doi.org/10.1166/jon.2021.1797.